Nature of lattice distortions in the cubic double perovskite Ba$_2$NaOsO$_6$

W. Liu,[1] R. Cong,[1] A. P. Reyes,[2] I. R. Fisher,[3,4] and V. F. Mitrović[1,*]

[1]*Department of Physics, Brown University, Providence, Rhode Island 02912, USA*
[2]*National High Magnetic Field Laboratory, Tallahassee, Florida 32310, USA*
[3]*Department of Applied Physics and Geballe Laboratory for Advanced Materials, Stanford University, California 94305, USA*
[4]*Stanford Institute for Materials and Energy Sciences, SLAC National Accelerator Laboratory,*
2575 Sand Hill Road, Menlo Park, California 94025, USA

We present detailed calculations of the electric field gradient (EFG) using a point charge approximation in Ba$_2$NaOsO$_6$, a Mott insulator with strong spin-orbit interaction. Recent ^{23}Na nuclear magnetic resonance (NMR) measurements found that the onset of local point symmetry breaking, likely caused by the formation of quadrupolar order [Chen, Pereira, and Balents, Phys. Rev. B **82**, 174440 (2010)], precedes the formation of long range magnetic order in this compound [Lu *et al.*, Nat. Commun. **8**, 14407 (2017); Liu *et al.*, Physica B **536**, 863 (2018)]. An extension of the static ^{23}Na NMR measurements as a function of the orientation of a 15 T applied magnetic field at 8 K in the magnetically ordered phase is reported. Broken local cubic symmetry induces a nonspherical electronic charge distribution around the Na site and thus finite EFG, affecting the NMR spectral shape. We combine the spectral analysis as a function of the orientation of the magnetic field with calculations of the EFG to determine the exact microscopic nature of the lattice distortions present in low temperature phases of this material. We establish that orthorhombic distortions, constrained along the cubic axes of the perovskite reference unit cell, of oxygen octahedra surrounding Na nuclei are present in the magnetic phase. Other common types of distortions often observed in oxide structures are considered as well.

I. INTRODUCTION

The investigation of the effects of spin orbit coupling (SOC) is one of the central issues in the study of quantum materials [1]. In addition to its key role in inducing topological phases, the combined effects of SOC and strong electronic correlations can lead to numerous emergent quantum phases [1–8]. A theoretical description of these phases is challenging. Certain approaches based on multipolar interactions have been proposed [2,7–9]. The key prediction of the quantum models with multipolar magnetic interactions is that a structural symmetry is lowered in the magnetically ordered phase. In fact for specific parameters, a quadrupolar/orbitally ordered phase precedes the formation of long range magnetism [2,7,9]. To provide tests of such theory one needs a probe that is concurrently sensitive to both orbital and spin degrees of freedom. Nuclear magnetic resonance (NMR) on nuclei with asymmetric charge distributions provide such tests, as was shown in Refs. [10,11]. In fact, in our recent ^{23}Na NMR measurements of the Mott insulator with strong spin-orbit interaction Ba$_2$NaOsO$_6$, we reported that the onset of local point symmetry breaking, likely caused by the formation of quadrupolar order, precedes the formation of long range magnetic order [10,11]. Specifically, we established that the magnetically ordered state is the exotic canted two-sublattice ferromagnet with broken local cubic symmetry. The broken local point symmetry (BLPS) phase that precedes magnetism is induced by deformations of oxygen

octahedra. We found that the BLPS extends over a wider temperature range as magnetic field increases, thus occupying a larger portion of the H-T phase diagram in high fields.

Here, we present an analysis of the angular evolution of NMR data as an applied magnetic field is rotated in different plains of the crystal. This analysis led us to conclude that the symmetry lowering transition is to an orthorhombic point symmetry. In crystals with cubic symmetry, the electric field gradient (EFG) vanishes. The lowering of the symmetry induces a finite EFG, which is a quantity directly observable in a static NMR measurement on a nuclei with finite quadrupole moment, such as ^{23}Na. Specifically, the parameter extracted from the spectra of such NMR experiments is the quadrupole resonance frequency, defined in terms of V_{zz}, which is the largest principal component of the EFG at the nuclear site, and other intrinsic nuclear properties [12–14]. Since the EFG tensor is a traceless rank-two tensor, its components can be determined by analysis of the spectra obtained as the orientation of the magnetic field is rotated with respect to the crystalline axes [12,15].

We use EFG calculations based on a point charge approximation [12] to describe how various local lattice deformations affect ^{23}Na spectra in Ba$_2$NaOsO$_6$. A comparison of these results with experimental findings allows us to determine the microscopic nature of local cubic symmetry breaking. In particular, we determine that the broken symmetry phase is characterized by the distortions of oxygen octahedra involving dominant displacement of oxygen ions along the cubic axes of the perovskite reference unit cell. Our work represents further demonstration of the power of NMR in exploring microscopic

*Corresponding author: vemi@brown.edu

properties [15–17], which in this case consist of probing spatial point symmetry breaking that spans well beyond its commonly known sensitivity to local magnetism [18].

The remainder of the paper is organized as follows. In Sec. II, we give a basic overview of the quadrupole interactions and present the ways in which these quadrupole effects are manifested in Ba$_2$NaOsO$_6$. We present the angle dependence of the quadrupole splitting, i.e., frequency difference between two adjacent quadrupole perturbed Zeeman energy levels, as applied magnetic field is rotated in two different planes of the crystal in Sec. III. In Sec. III A we present detailed analysis of the angular dependence data used to determine the exact symmetry of the EFG. The point charge approximation approach for calculating EFG is introduced in Sec. IV. Results of the point charge calculations for various distortion models are presented in Sec. V.

II. MANIFESTATION OF QUADRUPOLE EFFECT IN Ba$_2$NaOsO$_6$

The quadrupole effect refers to the interaction between the nonspherical nuclear charge distribution and an electrostatic field external to the nucleus. The nonspherical nuclear charge distribution appears in nuclei with spin $I > 1/2$ and is represented by the nuclear quadrupole moment $\hat{Q}$ operator, a second-rank tensor defined by the integral over the nuclear charge distribution [12]. This operator can be more conveniently expressed in terms of the nuclear spin operators I. In this case, its magnitude is proportional to what is conventionally referred to as the nuclear quadrupole moment eQ. The relevant electrostatic field, assuming a Laplacian potential, is represented by the EFG generated at the nuclear site by surrounding electronic charges [12,13]. Therefore, the strength of the quadrupolar interaction is dictated by the product of the nuclear quadrupole moment and the magnitude of the EFG. The nuclear quadrupole moment is nonzero for nuclei with spin $I > 1/2$, while the EFG is nonvanishing for point charges arranged on a lattice with symmetry lower than cubic. Thus, quadrupolar interactions generate finite effects only if $I > 1/2$ and the electronic charge distribution is asymmetric (noncubic).

In Fig. 1 we show a schematic of the energy levels for nuclei with spin $I = 3/2$, such as ^{23}Na that we investigated. Energy levels are displayed in both zero and a finite magnetic field H and in the presence of quadrupole interaction with the EFG. The resulting NMR spectra are also shown. As it was the case in our experiments, in a finite field we represent the quadrupolar interaction as a perturbation to the dominant Zeeman term. In zero applied field and in the presence of a finite EFG, a single line at a frequency proportional to the product of the nuclear quadrupole moment and the magnitude of the EFG can be observed in a nuclear quadrupole resonance (NQR) experiment. In a finite applied field and in the absence of quadrupolar interaction (i.e., EFG = 0), the spectrum consists of a single narrow line at the resonant frequency ω_0, which is proportional to the magnitude of the applied field. In the presence of quadrupolar interaction (i.e., EFG $\neq$ 0) the central transition remains at frequency ω_0. The satellite transitions appear at frequencies shifted by $\pm\delta_q$, which are proportional to the magnitude of the EFG (Appendix A). Thus, quadrupole
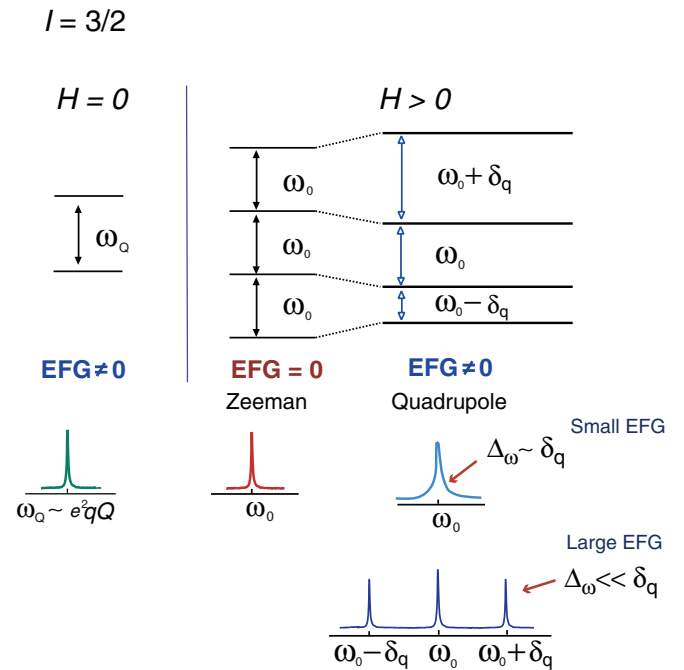

FIG. 1. Schematic of the energy levels for a $I = 3/2$ nucleus in both zero and a finite magnetic field H, in the presence of quadrupole interaction with the EFG generated by surrounding electronic charges, and the resulting NMR spectra. In principle, zero applied field and a finite EFG result in a single line at frequency ω_Q that can be observed in a nuclear quadrupole resonance (NQR) experiment. The frequency ω_Q is proportional to the product of nuclear quadrupole moment and the magnitude of the EFG. In a finite applied field and in the absence of quadrupole interaction, the spectrum consists of a single narrow line at frequency ω_0. In the presence of a quadrupole interaction that acts as a perturbation to dominant Zeeman Hamiltonian in the depicted case, the central transition remains at frequency ω_0. The satellite transitions appear at frequencies shifted by $\pm\delta_q$, which are proportional to the magnitude of the EFG [Eq. (2)]. For small values of the EFG, satellite transition cannot be resolved and only line broadening is observed. Strictly speaking, there is also a broadening due to the distribution of magnitude of the EFG itself, but this is manifested only on the satellites and not on the central transition.

interaction splits otherwise single NMR line to $2I = 3$ lines. Satellite transition cannot be resolved and only line broadening is observed for small values of the EFG.

These schematic qualitatives describe our ^{23}Na NMR observations in Ba$_2$NaOsO$_6$. The main effects of the quadrupole interaction observed in this compound are illustrated in Fig. 2. The high temperature, 20 K, paramagnetic state spectra consist of a single narrow NMR line. Since the nuclear spin for ^{23}Na equals to 3/2, the absence of the three distinct quadrupolar satellite lines indicates that the EFG is zero as a consequence of a cubic environment. Lowering the temperature broadens the NMR line (e.g., at 10.5 K) and eventually splits it into multiple peaks (e.g., at 4.2 K). This splitting indicating the start of significant changes in the local symmetry, thereby producing an EFG, i.e., asymmetric (noncubic) charge distribution. Therefore, the observed line broadening and subsequent splitting of the Na spectra into triplets in the magnetically ordered phase indicates breaking of the cubic point symmetry caused by local
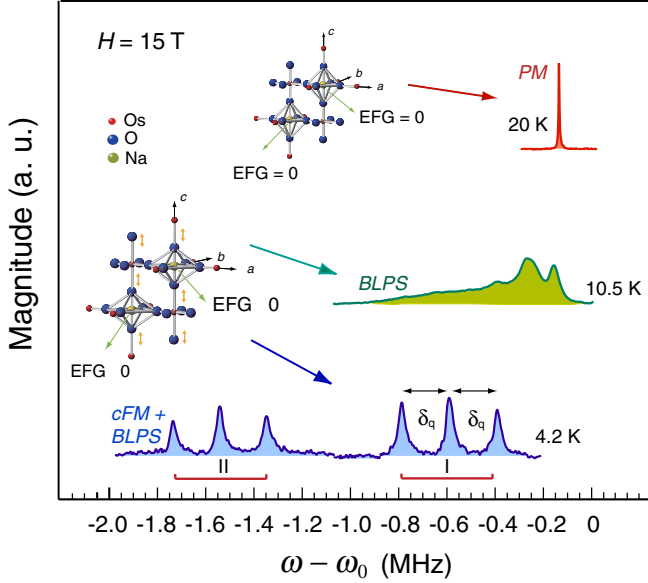
FIG. 2. Temperature evolution of ^{23}Na in Ba$_2$NaOsO$_6$ spectra at 15 T with magnetic field applied parallel to the [001] crystallographic axis. At 20 K, a narrow single peak spectrum characterizes the high temperature paramagnetic (PM) state. In this state, the crystal structure of Ba$_2$NaOsO$_6$ is undistorted, as depicted. That is, point symmetry at the Na site is cubic and leads to a vanishing EFG. At intermediate temperatures, broader and more complex spectra reveal the appearance of finite EFG induced by the breaking of local cubic symmetry. In this case, the crystal structure of Ba$_2$NaOsO$_6$ is distorted so that point symmetry at the Na site is noncubic, inducing a finite EFG. At lower temperature, the splitting into two sets of triplet lines (labeled as I and II) reflects the existence of two distinct magnetic sites in the lattice. Zero of frequency is defined as $\omega_0 = {}^{23}\gamma\,H$. Splitting between quadrupolar satellites is denoted by δ_q. Abbreviation: PM, paramagnetic; BLPS, broken local point symmetry; cFM, canted ferromagnetic.

distortions of electronic charge distribution, as established in Refs. [10,11]. The data was taken in the same experimental conditions as described in detail in Ref. [11]. At 4.2 K, the ^{23}Na spectra clearly split into six peaks. These peaks correspond to two sets of triplet lines, labeled as I and II in Fig. 2, that are well separated in frequency. As previously established, these two sets of triplets appear due to magnetic interactions [10] that are irrelevant to our discussion of quadrupole effects. The splitting labeled δ_q in Fig. 2 implies that a finite EFG has been induced by changes in local charge distribution. In this paper we will consider various modifications of local lattice symmetry that can induce a finite EFG and account for our experimental observations [10,11]. However, we first give a more quantitative overview of the quadrupole interaction.

For anisotropic charge distributions, the quadrupole Hamiltonian expressed in the coordinate system define by the principal axes of the EFG is given by

$$\mathcal{H}_Q(x,y) = \frac{eQ V_{zz}}{4I(2I-1)}\left[(3\hat{I}_z^2 - \hat{I}^2) + \eta(\hat{I}_x^2 - \hat{I}_y^2)\right], \quad (1)$$

where eQ is the quantity conventionally referred to as the nuclear quadrupole moment, $\eta \equiv (V_{xx} - V_{yy})/V_{zz}$ is the asymmetry parameter, and V_{xx}, V_{yy}, and V_{zz} are diagonal

components of the EFG. Here, $V_{zz} \equiv eq$ is defined as the principle component of the EFG and $|V_{xx}| \leqslant |V_{yy}| \leqslant |V_{zz}|$, by convention [18]. The EFG is a symmetric and traceless 3×3 tensor that corresponds to the rate of change of the electric field at an atomic nucleus [19]. The principal axis of the EFG defines the coordinate system O_{XYZ}, which is not necessarily aligned with that defined by the crystalline axes O_{xyz}. Evidently, V_{zz} is parallel to one of the crystal axes if the principal axes of the EFG and those of the crystal are aligned.

We define the observable δ_q to represent the quadrupole splitting between different quadrupole satellites. As derived in Appendix A, δ_q corresponds to the frequency difference between adjacent quadrupole satellite transitions. In the most general case the quadrupole splitting δ_q is given by

$$\delta_q = \frac{(eQ)(V_{zz})}{2h}\left(1 + \frac{\eta^2}{3}\right)^{1/2}. \quad (2)$$

Thus, the value of δ_q is dictated by both the magnitude of the principal component of the EFG (V_{zz}) and the anisotropy parameter η. In the high field limit, when $\mathcal{H}_Q$ is a perturbation to the dominant Zeeman term, the angular dependence of the splitting is given by

$$\delta_q = \frac{\nu_q}{2}(3\cos^2\theta - 1 + \eta\sin^2\theta\cos 2\phi), \quad (3)$$

where θ is the angle between the applied field H and V_{zz}, ϕ is the standard azimuthal angle of a spherical coordinate system defined by O_{XYZ}, and $\nu_Q \equiv \frac{(eQ)V_{zz}}{2h}$. Therefore, to test whether an observed splitting in the NMR spectra originates from quadrupole effects, one has to measure the spectra as a function of strength and orientation of the applied magnetic field. Clearly, for a fix orientation of the applied field the splitting should be independent of its magnitude. As a matter of fact, we establish that δ_q varies by $\leqslant 2\%$, which is of the order of the error bars, as H increases from 7 T to 29 T [11]. Insensitivity of δ_q to the strength of the magnetic field implies that the splitting originates from quadrupole effects. Namely, the finite EFG is induced by changes in charge density distribution and/or lattice distortions and not by trivial magnetostriction effect on a crystal. However, to decipher the detailed structure of the EFG tensor, one has to investigate how δ_q evolves as the orientation of the applied field is varied with respect to crystalline axes. As we will describe in detail in the next section, this type of rotational studies allows us to discern the exact nature of the distortions.

III. ANGULAR DEPENDENCE OF QUADRUPOLE EFFECT

We performed detailed measurements of δ_q at 15 T and 8 K as a function of the angle (θ) between H and the [001] crystalline axis in two different planes of the crystal [(1$\bar{1}$0) and (010)]. The measured angle dependence of the splitting is plotted in Fig. 3. We observe that the splitting between any two adjacent peaks of the triplets I and/or II is equal, within the error bars. Therefore, we plot the mean peak-to-peak splitting between any two adjacent peaks of the triplets I and II. We observed that the splitting is the largest for $H\parallel$[001]. Moreover, for rotations in the (010) plane, i.e., along one face of the cubic unit cell, we find that δ_q reaches its maximum value for $H\parallel$[100] as well [20]. Furthermore as described in Ref. [10],
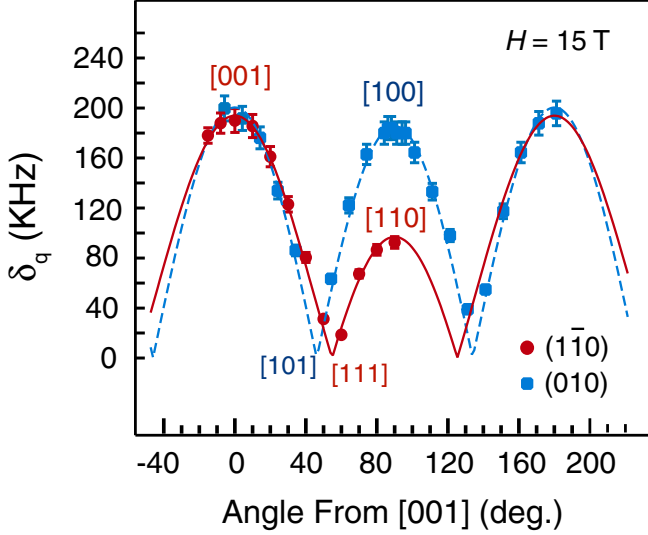
FIG. 3. The mean peak-to-peak splitting (δ_q) between any two adjacent peaks of the triplets I and II as a function of the angle between [001] crystal axis and the applied magnetic field (H). The red circles denote angular dependence of splitting for H rotated in the ($1\bar{1}0$) plane. The red solid line is the fit to $|(3\cos^2\theta - 1)/2|$, where θ denotes the angle between the principal axis of the EFG (V_{ZZ}) and the applied magnetic field. The blue squares denote the angular dependence of splitting when the sample is rotated in the (010) plane. The blue dotted line is the fit to $|(3\sin^2\theta - 1 - \eta\cos^2\theta)/2|$ [Eq. (14)], where θ denotes the angle between the (V_{ZZ}) and H, and η is the asymmetric parameter as explained in the text.

we observe no more than three lines per set (I or II) regardless of the angle θ. This indicates that the magnetic field was rotated in the coordinate system defined by the principal axes of the EFG. In other words, the principal axes of the EFG must coincide with those of the crystal in a low temperature noncubic phase of Ba$_2$NaOsO$_6$. This observation together with finding equal δ_q on triplets I and II, i.e., two magnetically inequivalent Na sites, implies that in the simplest scenario the finite EFG arises from distortions of the O^{2-} octahedra surrounding Na$^+$ ions with the oxygen constrained to move along the cubic axes of the perovskite reference unit cell, as illustrated in Fig. 2.

In a material with global cubic symmetry such as Ba$_2$NaOsO$_6$, it is thus possible to stabilize three different domains, each with the principle axis of the EFG, V_{zz}, pointing along any of the three equivalent crystal axes. The fact that the splitting is the largest for $H\|$[001], and that only three peaks per set are observed for $H\|$[110], implies that two domains are plausible in the crystal. One domain is characterized by pure uniaxial $3z^2 - r^2$ distortions where V_{zz} is in the [001] direction, while the other is distinguished by $x^2 - y^2$ distortions where V_{zz} is in the (110) plane. In the simplest case V_{zz} is parallel to the [001] direction with $\eta = 0$, indicating tetragonal local symmetry. In the second case, V_{zz} is aligned along the [100] direction with η of order 1, implying orthorhombic local symmetry. To determine the exact local symmetry, i.e., distinguish between tetragonal and orthorhombic distortions, we need to consider the details of the angular dependence of the splittings δ_q obtained for rotations of the applied field in the (010) plane. The fact that δ_q reaches its maximum value for both

$H\|$[001] and $H\|$[100], for the field rotated in the the (010) plane, reveals orthorhombic local symmetry. Next, we discuss in detail the claim that our observations imply orthorhombic local symmetry.

Tetragonal symmetry vs orthorhombic symmetry

To qualitatively analyze δ_q as the magnetic field is rotated, we start by transforming the Hamiltonian in Eq. (1) into the coordinate system O_{xyz}, defined by H having the O_z axis parallel to the applied field. Assuming that the local symmetry is tetragonal, that is $V_{xx} = V_{yy}$ and $\eta = 0$, and that V_{zz} is parallel to the crystalline c axis, we may without loss of generality choose the axis, O_z parallel to the applied magnetic field H in plane XOZ, so that

$$I_Z = I_z \cos\theta + I_x \sin\theta, \tag{4}$$

where θ is the angle between H and V_{zz}. Then, the quadrupole Hamiltonian in O_{xyz} becomes

$$\mathcal{H}_Q = \frac{1}{6}h\nu_Q\left\{\frac{1}{2}(3\cos^2\theta - 1)\left(3I_z^2 - I(I+1)\right)\right.$$
$$+ \frac{3}{2}\sin\theta\cos\theta[I_z(I_+ + I_-) + (I_+ + I_-)I_z]$$
$$+ \left.\frac{3}{4}\sin^2\theta(I_+^2 + I_-^2)\right\}, \tag{5}$$

where $\nu_Q = \frac{3e^2qQ}{2hI(2I-1)}$.

Taking the quadrupole Hamiltonian as a perturbation to the dominant Zeeman term, the energy eigenstates of $\mathcal{H}_Q$ are given by

$$E_m = \frac{1}{12}h\nu_Q[3m^2 - I(I+1)](3\cos^2\theta - 1). \tag{6}$$

The quadrupole splitting δ_q between adjacent quadrupole satellites then equals to

$$\delta_q = \frac{E_m - E_{m-1}}{h} = \frac{1}{2}\nu_Q(3\cos^2\theta - 1) \tag{7}$$

Equation 7 describes the angular dependence of quadrupole splitting in the case of tetragonal symmetry ($\eta = 0$) and V_{zz} parallel to the c axis. We observe such angular dependence when H is rotated from the [001] to [110] direction, i.e., in the ($1\bar{1}1$) plane, as shown in Fig. 3.

If η is not confined to be zero, one deduces a more general form of the energy eigenstates of $\mathcal{H}_Q$ [18],

$$E_m = \frac{1}{12}h\nu_Q[3m^2 - I(I+1)]$$
$$\times [(3\cos^2\theta - 1) + \eta\sin^2\theta\cos 2\phi], \tag{8}$$

leading to

$$\delta_q = \frac{E_m - E_{m-1}}{h}$$
$$= \frac{1}{2}\nu_Q(3\cos^2\theta - 1 + \eta\sin^2\theta\cos 2\phi), \tag{9}$$

where angles θ and ϕ are as defined in Fig. 4. For the applied field rotated in the ($1\bar{1}0$) plane, as was the case in one of our measurements, $\cos 2\phi = 0$, as illustrated in Fig. 4(a). Then, fitting our data for angular dependence of δ_q as H is rotated in the ($1\bar{1}0$) plane to Eq. (9), for $V_{zz}\|c$, we obtain that either $\eta = 0$ for tetragonal symmetry or $\eta \neq 0$ for orthorhombic symmetry.

Up to this point, we have assumed that V_{zz} is parallel to the c axis. We point out that the splitting δ_q, as derived in all of the above equations, depends on polar angles θ and ϕ that are given
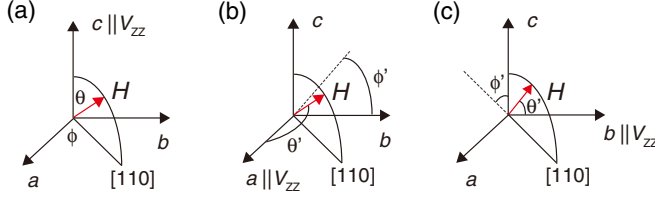
FIG. 4. Schematic of rotation of the applied field in the $(1\bar{1}0)$ plane. The red arrow denotes the applied field direction. V_{ZZ} is parallel to c, a and b axis in (a), (b), and (c), respectively.

FIG. 5. Schematic of rotation of the applied field in the (010) plane. The red arrow denotes the applied field direction. V_{ZZ} is parallel to the c, a, and b axis in (a), (b), and (c), respectively.

in the coordinate system defined by the principal axes of the EFG. When V_{zz} is parallel to the c axis, the coordinate system defined by the principal axes of the EFG coincides with that defined by crystalline axes. However, if V_{zz} is parallel to the a or b axis as depicted in Figs. 4(b) and 4(c), θ and ϕ need to be transformed into crystalline coordinates. This transformation is necessary for a meaningful comparison with the data as only the orientation of H with respect to crystalline axes is know in an experiment. We denote angles θ' and ϕ' [which are θ and ϕ in Eq. (9)] as angles defined in the EFG coordinate system. These angles are related to the angles θ and ϕ in the crystalline coordinate system according to the following transformations,

$$\cos\theta' = \sin\theta\cos\phi$$
$$\sin\theta'\cos\phi' = \sin\theta\sin\phi$$
$$\sin\theta'\sin\phi' = \cos\theta, \qquad (10)$$

for $V_{zz}\|a$ and

$$\cos\theta' = \sin\theta\cos\phi$$
$$\sin\theta'\cos\phi' = \cos\theta$$
$$\sin\theta'\sin\phi' = \sin\theta\sin\phi, \qquad (11)$$

for $V_{zz}\|b$ axis. When the applied magnetic field is rotated in the $(1\bar{1}0)$ plane $\phi = 45°$, as shown in Fig. 4(b), Eq. (9) becomes

$$\delta_q = \frac{1}{2}\nu_Q\left(\frac{3}{2}\sin^2\theta - 1 - \eta\left(\frac{3}{2}\cos^2\theta - \frac{1}{2}\right)\right). \qquad (12)$$

Evidently, fitting the angular dependence of δ_q for H rotated in the $(1\bar{1}0)$ plane to Eq. (12) produces the same quality fitting curve as a fit to Eq. (9) but with $\eta \approx 0.87$. The nonzero value of η indicates that the symmetry is lower than tetragonal. Moreover, as V_{zz} is parallel to either the a or b axis, symmetry must be orthorhombic.

Thus far, both the tetragonal symmetry [with either V_{zz} parallel to the c axis or the b axis] and orthorhombic symmetry (with V_{zz} parallel to the a or c axis) EFG could account for the observed angular dependence of δ_q when H is rotated in the $(1\bar{1}0)$ plane. Clearly, in orthorhombic structure, C4 rotation symmetry is broken and the oxygen octahedra are distorted so that $a \neq b \neq c$. To determine undeniably whether distortions (i.e., EFG) are tetragonal or orthorhombic, we performed another measurement of the angular dependence of the splitting in which the applied field was rotated in the (010) plane. To understand these results, plotted in Fig. 3, we consider different orientations of V_{zz} as shown in Fig. 5.
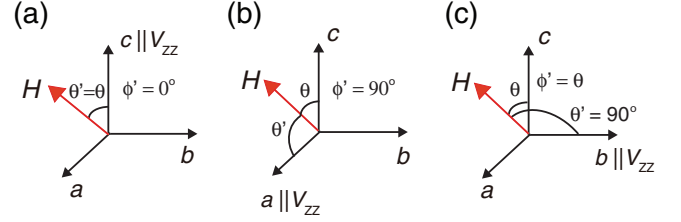
First, assuming that V_{zz} is parallel to the c axis, $\theta' = \theta$ and $\phi' = 0$, so that Eq. (9) becomes

$$\delta_q = \frac{1}{2}\nu_Q(3\cos^2\theta - 1 + \eta\sin^2\theta). \qquad (13)$$

If on the other hand V_{zz} is parallel to the a axis, we obtain $\theta' = 90° - \theta$ and $\phi' = 90°$. The angular dependence of splitting is given by

$$\delta_q = \frac{1}{2}\nu_Q(3\sin^2\theta - 1 - \eta\cos^2\theta). \qquad (14)$$

Finally, if V_{zz} is parallel to the b axis, we have $\theta' = 90°$ and $\phi' = 0$. The splitting becomes

$$\delta_q = \frac{1}{2}\nu_Q(\eta\cos 2\theta - 1). \qquad (15)$$

The observed angular dependence of δ_q for H rotated in the (010) plane can only be fit to Eq. (14). In this case, the fitting yields $\eta \approx 0.87$.

To sum up, the observed angular dependence of the splitting confirms that such splitting is due to quadrupole effect. Since no more than three lines per set (I or II) are observed regardless of the angle θ, the principal axes of the EFG must coincide with those of the crystal. Furthermore, we found that distortions with both tetragonal [with V_{zz} parallel to the c axis or the b axis] and orthorhombic symmetry (with V_{zz} parallel to either the a or c axis) could account for angular dependence of the splitting for H rotated in the $(1\bar{1}0)$ plane. However, only orthorhombic distortions (with V_{zz} parallel to the a axis) could explain the angular dependence of the splitting δ_q for H rotated in the (010) plane. Therefore, by combining the results of the angular dependence of δ_q for H rotated in two different planes, we conclude that the distortion is orthorhombic with $\eta \approx 0.87$ and $V_{zz}\|a$. Because the well defined splitting is observed solely in the low temperature magnetically ordered phase, we can undeniably deduce that orthorhombic distortions are present in that low temperature phase. In high temperature BLPS, i.e., paramagnetic, phase we do not detect well defined splitting but rather convoluted broadening. Therefore, since the exact dependence of δ_q on the field orientation is unknown, dominant tetragonal distortions along the [001] direction can in principle account for the line broadening in the PM phase. Furthermore as described in Ref. [10], in the BLPS phase the width of the NMR spectra allows us to place an upper limit on these distortions. We established that any deformations that exceed 0.02% of the respective lattice constant would cause visible broadening/splitting of the NMR spectra in the PM state. In fact, x-ray scattering measurements provide evidence of tetragonal distortions at higher temperature paramagnetic phase [21]. These distortions, though extremely small, become

significant below 100 K. However, they do not exceed the limit of resolution of 0.02% of the respective lattice constant in our experiment and thus cause no detectable broadening/splitting of the NMR spectra.

As we described, in a material with global cubic symmetry, it is possible to stabilize three different domains, each with the principle axis of the EFG, V_{zz}, pointing along any of the three equivalent crystal axes. Therefore, for either a cubic to orthorhombic, or a tetragonal to orthorhombic phase transition, formation of distinct domains, with their principle axes rotated by 90 degrees, is expected. The analysis of the angular dependence of the spectral lineshapes in the low temperature magnetic phase did not provide any evidence for the formation of different domains. Thus, this must imply the presence of some weak symmetry-breaking field that favors one domain over the others. A possible source of such a symmetry breaking field is provided by the strain from the way the sample was mounted on the flat platform, which was always parallel to the specific face of the crystal. We emphasize that the distortions described here are of local nature, involving oxygen octahedra that surround Na sites. In principle, it is possible to preserve global cubic symmetry, even in the presence of such local distortions, in a double-perovskite structure.

IV. POINT CHARGE APPROXIMATION

We employed the point charge model to calculate V_{ZZ} and η resulting from different distortion scenarios. This is done to find the full set of possible distortions that can account for our observations, i.e., maximum splitting equals $\delta_q \approx 190$ kHz, for $H \| c$ for all satellite transitions, $\eta \approx 0.87$, and $V_{ZZ} \| a$. In this model, the electron density at the Na site is calculated by taking into account all the surrounding charges, which are treated as the point charges of zero radius that carry the appropriate ionic charge. The surrounding charges are accounted for by a lattice summation method that is easily employed for systems with a large number of atoms and/or single crystals. We note that the point-charge approximation of ions neglects any covalent nature of the bonding in a material and is therefore strictly valid in strongly ionic compounds, which is the case in Ba_2NaOsO_6. In fact, the double-perovskite structure of Ba_2NaOsO_6 is an example of a heptavalent osmium compound with Os^{+7}. The Fermi level lies within the $t2g$ bands, confirming the heptavalent nature of the Os ion [24]. Nevertheless, formal valence of +7 for Os does not represent a real charge on the Os ion, due to strong mixing of Os and O molecular orbitals [22]. For computational simplicity we have adopted a point charge model in which the Os carries a charge of +7, though this is clearly an approximation given the mixed Os and O character of the molecular orbitals. Therefore, for the purpose of our calculation, we assigned the following charges to each of the ions: Os^{7+}, Ba^{2+}, Na^{1+}, and O^{2-}.

The EFG tensor components V_{ij}, $i, j = x, y, z$, at a certain nuclear site resulting from an ion of charge q are given by [25]

$$V_{ij} = \sum_{\mu} \sum_{k} q_k \frac{3(^k r_i^\mu)(^k r_j^\mu) - \delta_{ij}(^k r^\mu)^2}{(^k r^\mu)^5}, \quad (16)$$

where $\sum_{\mu}$ denotes the sum over multiple unit cells, and $\sum_{k}$ is the sum over all atoms within a single unit cell, and r is the

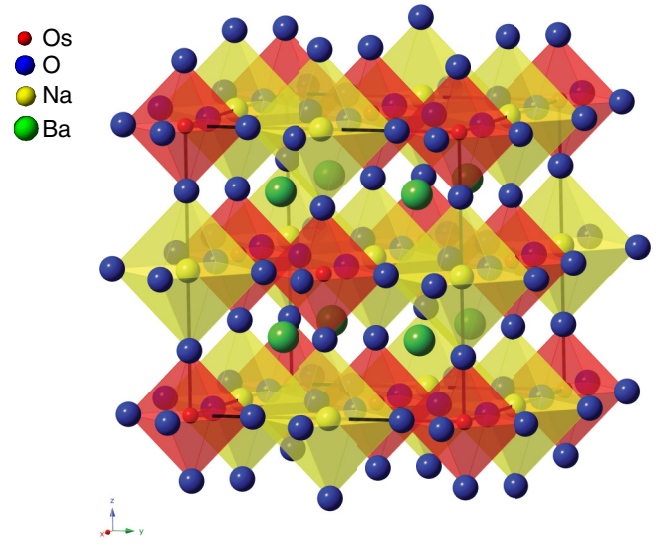

FIG. 6. Crystal structure of Ba_2NaOsO_6 deduced from x-ray diffraction at room temperature [22,23]. Solid lines show the unit cell. Oxygen, osmium, and sodium ions form face centered cubic structure, while barium ions arrange a simple cubic structure. This undistorted double-perovskite structure has $Fm\bar{3}m$ space group.

distance from the specific nuclear site, the point of interest, to the ion being considered. This expression is summed over all ions in the structure that contributes to the EFG tensor at the point of interest. Since the EFG is a two-dimensional tensor with nine elements, each element V_{ij} represents a second derivative with $i, j \subset X, Y, Z$. The EFG tensor is then diagonalized to obtain the principal components V_{xx}, V_{yy}, and V_{zz}, where, by convention, $|V_{xx}| \leqslant |V_{yy}| \leqslant |V_{zz}|$. The principal components are then used to calculate the observables, the asymmetry parameter $\eta \equiv (V_{xx} - V_{yy})/V_{zz}$ and the splitting $\delta_q = \frac{1}{2h}(eQ)(V_{zz})$, where eQ is the nuclear quadrupole moment. We point out that our approach cannot reproduce the EFG tensor quantitatively with high fidelity. However, it can reliably identify symmetry breaking distortions.

We can then calculate the EFG tensor at any nuclear site by numerically summing over the lattice for any known crystal structure. The crystal structure of Ba_2NaOsO_6 is shown in Fig. 6. At room temperature this material has an undistorted double-perovskite structure, in which OsO_6 octahedra are neither distorted nor rotated with respect to each other or the underlying lattice. Specifically, considering the periodic nature of crystal structure, one determines the lattice in a standard way by translation of the three primary vectors, as described in detail in Appendix B. Since EFG elements are proportional to $1/r^3$, we found that an iteration over 64 unit cells suffices to make numerical results converge. That is, summing beyond 64 unit cells does not induce variations in the mean value of any observable that exceed 1%. More precisely, we compared the results of summations ranging over up to 8000 unit cells. In each unit cell, there are 89 ions and the position of each ion can be accessed by Eq. (B3).

The first step of the numerical calculation is to set up the distortion model. We emphasize that we cannot distinguish between displacements of the actual ions and distortions of

the ion charge density in our measurements. Moreover, the point-charge method does not permit modeling distortions of the ion charge density. Therefore, we choose to model the development of the final EFG by local distortions only. The local distortion of oxygen ions in an NaO_6 octahedron is reflected by altering the basis indices. For example, in order to test the effect of 2%'s elongation along the c axis of the oxygen ion above the Na site at origin, its original position $(0,0,0.25a)$ should be modified to $(0,0,0.25(1+2\%)a)$, where a is the lattice constant. After laying out the distortion model of a single unit cell, we iterate over all unit cells by changing primary vectors. In each unit cell, we first access the position and charge of each ion and then calculate all the EFG elements. Finally, after the iterations, we calculate the asymmetry parameter $\eta \equiv (V_{xx} - V_{yy})/V_{zz}$ and maximum $\delta_q \equiv \frac{1}{2h}(eQ)(V_{zz})$ (for $H \| c$), as derived in Eq. (A4). Moreover, even though the calculation can yield V_{zz} parallel to either the a or b crystal axes for orthorhombic distortions, our measurements presented here do not allow us to discern between these two orientations of V_{zz}. Therefore, we use symmetry arguments to compare results of calculations to our measurements.

V. RESULTS AND DISCUSSIONS OF POINT CHARGE CALCULATIONS

Next, we describe results of our calculations of the EFG induced by various types of distortions using the point charge approximation. We first consider distortions where the oxygen ions, forming the O^{2-} octahedra surrounding Na^+ ions, are constrained to move along the cubic axes of the perovskite reference unit cell.

A. Distortion along the principal axis—one structurally distinct Na site

This model involves distortions of the O^{2-} octahedra surrounding Na^+ ions as illustrated in Fig. 7(a). We assume that the modifications are identical for all the octahedra and that three pairs of O ions independently move along each crystalline axis. That is, each pair of O ions can either elongate or compress symmetrically about the central Na site by an arbitrary amount along the Na-O bond direction. We note that we are not making any prior assumptions about the structural symmetry. The schematic of this model is shown in Fig. 7(a). In the actual simulation we define the distortion in percentage relative to the Na-O distance, 2.274 Å, of the undistorted bond. We also define the elongation deformation as negative and the compression deformation as positive.
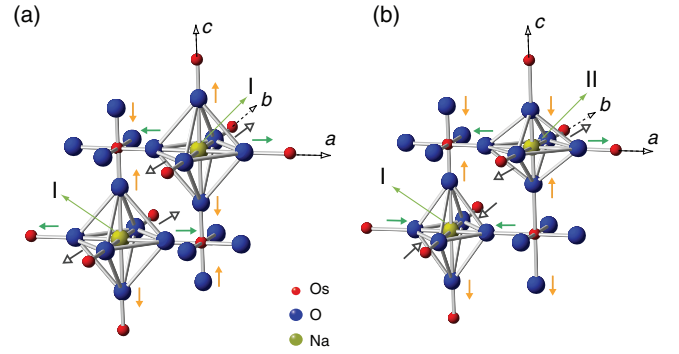

FIG. 7. Schematic of the proposed lattice distortions. (a) One structurally distinct Na site in a noncubic environment is produced by elongation/compression of O^{2-} octahedra. (Model A) (b) Two structurally distinct Na sites are generated by elongation, or compression, of one O^{2-} octahedron along the [001] direction and its concurrent compression, or elongation, in the (a,b) plane. (Model B)

The simulation is ran to produce combinations of distortions along all three axes of the original cubic axes of the perovskite reference unit cell which can reproduce our observations. Thus, our parameter space consists of three numbers, δ_a, δ_b, and δ_c, corresponding to distortions along crystalline a, b, and c axes, respectively. We find that numerous combinations result in the desired/observed values of δ_q and η, some of which are listed in Table I. v_{aa}, v_{bb}, and v_{cc} are the EFG components along the a, b, and c axis of the lattice coordinate, and $V_{zz} \equiv \frac{e}{4\pi\epsilon_0}\frac{1}{a^3}v_{zz}$ (here a is the lattice constant) is the largest absolute value of the three by definition.

As evident in Table I, orthorhombic distortions with $\eta \approx 0.87$ can induce the desired value of δ_q for different values of relative displacement along any of the three crystalline axes. In addition to the appropriate value of δ_q, the calculations have to identify a set of relative displacements that generate the EFG with its principal component along the a axis to account for the data. The set of displacements that account for our experimental observations are presented in bold font in Table I. We find that distortion along any particular direction that does not exceed 0.8% of the respective lattice constant reproduces the EFG parameters, in agreement with our observations.

B. Distortion along principal axis—two structurally distinct Na sites

In this second model, two structurally different Na sites are generated by elongation, or compression, of one O^{2-} octahedron along the [001] direction and its concurrent compression, or elongation, in the (110) plane, as illustrated in Fig. 7(b).

TABLE I. Sample results of point charge calculations with one structurally Na site. Program loops through δ_a, δ_b, and δ_c values within the range of $(-5\%, 5\%)$ and returns combinations of parameters that can yield η in the vicinity of 0.87 and $\delta_q \approx 190$ kHz. The parameters that reproduce our experimental findings are in bold fonts. (Model A)

δ_a	δ_b	δ_c	η	v_{aa}	v_{bb}	v_{cc}	δ_q(kHz)	V_{zz}
0.1%	0.55%	0.25%	0.87	−2.39	38.89	−36.49	189.8	$b\,(y)$
0.55%	**0.1%**	**0.2%**	**0.87**	**38.89**	**−2.395**	**−36.49**	**189.8**	**a (x)**
−0.25%	−0.65%	−0.1%	0.87	2.394	−38.89	36.49	189.8	$c\,(z)$
−0.65%	**−0.25%**	**−0.1%**	**0.87**	**−38.89**	**2.394**	**36.49**	**189.8**	**a (x)**

TABLE II. Sample results of point charge calculations with two structurally distinct Na sites. (Model B)

δ_a	δ_b	δ_c	η	v_{aa}	v_{bb}	v_{cc}	δ_q(kHz)	V_{zz}
−0.185%	−0.185%	0.185%	0	27.9	27.9	−55.9	190.03	$c\,(z)$
0.185%	0.185%	−0.185%	0	−27.9	−27.9	55.9	190.03	$c\,(z)$

This model also naturally accounts for the appearance of two magnetically different Na sites. These two sites appear from the two distinct frequency shifts for triplet I and II, even if the magnetically ordered state is a simple ferromagnet where all spins on Os^{7+} ions are assumed to point in the same direction. The transfer hyperfine field from Os electronic spins to the Na nuclei is mediated by O^{2-} ions via its p-d hybridization with a well localized $5d$ orbital of Os^{7+}. Evidently, the shorter the distance between O^{2-} and Os^{7+} ions, the stronger the hybridization and thus transfer hyperfine field at the Na site. Thus, the internal field at the Na site in the lower plane [in Fig. 7(b)] consists of a sum of two stronger and four weaker fields, while the field at Na in the upper plane consists of a sum of four stronger and two weaker fields. Consequently, NMR signal from the lower plane Na will appear at smaller absolute frequency shift (as is the case for triplet I), while that from the upper plane will appear at the larger absolute frequency shift (triplet II) (Table II).

The findings of our point charge simulations indicate that in order to generate equal δ_q for both Na sites, as we established in our experiments, the relative magnitude of the elongation has to be equal to that of the compression, i.e., distortions must satisfy the relation $|\delta_a| = |\delta_b| = |\delta_c|$. It is very unlikely that such distortions will occur, as electrostatic energies associated with elongation and compression of the octahedra by the same relative amount are very different. However, as it results from our calculations, such distortions are of tetragonal symmetry and can only induce $\eta = 0$, in contrast to our observations. For the reasons listed, this model cannot account for our data.

C. Rotational distortion in the (a,b) plane

Here we consider model C, consisting of rotations of oxygen ions in the (110) plane. In this model for each Na, four of its surrounding O^{2-} ions in the (a,b) plane undergo a counterclockwise rotation, as viewed from the top and depicted in Fig. 8. We found that our calculations could not generate the splitting δ_q of 190 kHz, as shown in Table III. More importantly, only tetragonal distortions with $\eta = 0$ are generated, which is inconsistent with our data as well.

TABLE III. Sample results of point charge calculations of rotational distortion in the (a,b) plane. (Model C)

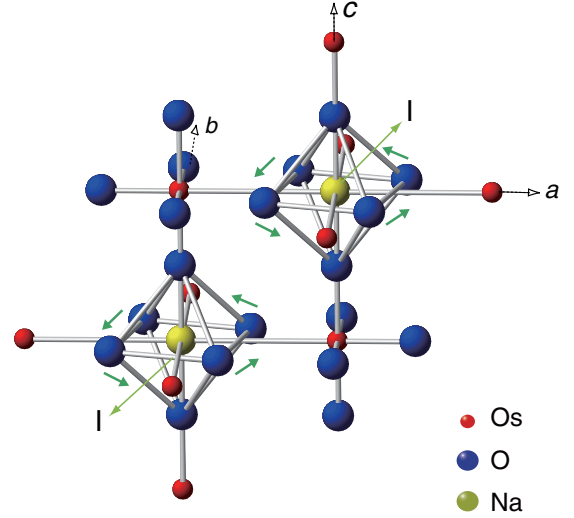| ϕ	δ_c	η	v_{aa}	v_{bb}	v_{cc}	δ_q(kHz)	V_{zz}
5°	0%	0	−0.6675	−0.6675	1.335	4.899	c
25°	0%	0	−12.09	−12.09	24.19	88.764	c
45°	0%	0	−20.65	−20.65	41.3	151.57	c
65°	0%	0	−12.09	−12.09	24.19	88.764	c
85°	0%	0	−0.6675	−0.6675	1.335	4.899	c

FIG. 8. Schematic of the rotational lattice distortion generating single Na site. One structurally distinct Na site in noncubic environment is produced by in-plane rotation of O^{2-} octahedra, as depicted by shorter green arrows. (Model C)

Next, we add distortions that involve the other two O^{2-} (Fig. 9). Simple arguments indicate that this type of proposed distortion possesses tetragonal symmetry, i.e., $\eta = 0$. In Table IV we display distortions that generate the observed splitting in point charge simulations. Calculations indicate that this model only generates tetragonal distortions with $\eta = 0$ and $V_{zz} \| c$, both inconsistent with our experimental findings. Therefore, both models with dominant rotational distortions in the (a,b) plane fail to account for our data.
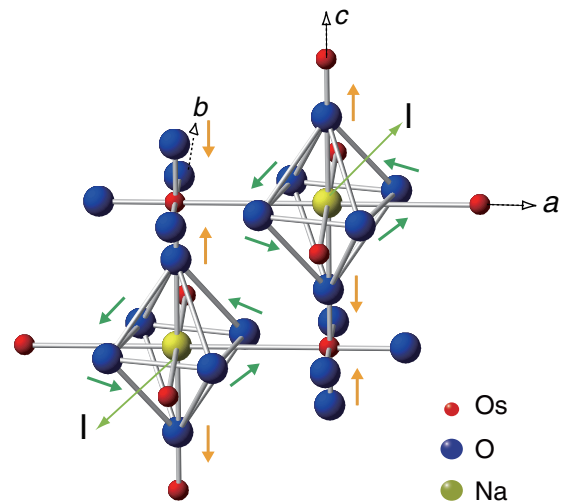

FIG. 9. Schematic of the rotational lattice distortion combined with elongation, or compression, of two oxygen ions along the [001] direction. One structurally distinct Na site in noncubic environment is produced by this lattice modification, consisting of in-plane rotation (green arrows) and distortion along the c axis (orange arrows) of O^{2-} octahedra. (Model C_2)

TABLE IV. Sample results of point charge calculations of rotational distortion in the (a,b) plane with c-axis elongation or compression. Positive values in the δ_c column represent compression while negative ones represent elongation. (Model C_2)

δ_c	ϕ	η	v_{aa}	v_{bb}	v_{cc}	δ_q(kHz)	V_{zz}
1%	20°	0	26.18	26.18	−52.35	192.13	c
0.9%	15°	0	25.8	25.8	−51.59	189.34	c
−0.2%	40°	0	−26.35	−26.35	52.69	193.38	c
−0.25%	35°	0	−26.09	−26.09	52.18	191.51	c
−0.35%	30°	0	−26.4	−26.4	52.81	193.8	c
−0.45%	25°	0	−26.06	−26.06	52.12	191.29	c
−0.85%	5°	0	−26.29	−26.29	52.59	193	c

D. Tilt distortion in the (a,c) plane

In the following model, we consider tilt distortions in the (a,c) plane depicted in Fig. 10. Two O^{2-} ions of the octahedra position along the c axis are tilted by an angle θ away from the c axis in the (a,c) plane. The rest of the crystal remains unchanged. Since this tilt does not involve the entire octahedra, it does not represent Glazer-type distortion, as explained in Appendix C. To generate the observed splitting, the tilt angle θ is found to be $\approx 10°$. However, the resulting asymmetry parameter is ≈ 0.69, as shown in Table V. This value of η is insufficient to account for the experimental data.

E. Rotational distortion in the (a,b) plane and tilt distortion in the (a,c) plane

In this model, we consider tilt distortions in the (a,c) plane accompanied by a rotational distortion in the (a,b) plane, as described in Model C. Specifically, the lattice modification consists of a rotational distortion in the (a,b) plane and a tilt in the (a,c) plane, as shown in Fig. 11. Four O^{2-} ions

TABLE V. Sample results of point charge calculations of tilt distortion in the (a,c) plane. (Model D)

θ	η	v_{aa}	v_{bb}	v_{cc}	δ_q(kHz)	V_{zz}
10°	0.6877	−41.46	6.473	34.99	184.67	a
10.1°	0.6888	−41.97	6.529	35.44	187.03	a
10.2°	0.6899	−42.48	6.586	35.9	189.41	a
10.3°	0.691	−43	6.644	36.36	191.82	a
10.4°	0.692	−43.52	6.702	36.82	194.25	a
10.5°	0.6931	−44.05	6.76	37.29	196.7	a

of octahedra positioned in the same plain as Na, i.e., in the (a,b) plane, are rotated by an angle ϕ (counterclockwise from the a axis). The two remaining O^{2-} ions, located along the c axis, are tilted by an angle θ relative to the c axis. A subset of angles θ and ϕ that generate parameters, in point charge approximation, in agreement with experimental observations are listed in Table VI. We find that for $\theta = 8.5° \pm 0.4°$ and $\phi = 12° \pm 1°$ calculations results are in good agreement with our data. Therefore, this is the only model in addition to Model A that well accounts for our observations.

F. Common lattice distortions in perovskite oxides

Perovskite oxides are well known to be prone to lattice distortions [26,27]. However the tolerance factor, an indicator for the stability of crystal structures, of Ba_2NaOsO_6 is 0.99, which falls in to the very stable category for cubic structure [22].

Nevertheless, in this section we consider common lattice instabilities often present in perovskite transition metal oxides, with tolerance factors less than 0.98. In general, these lattice
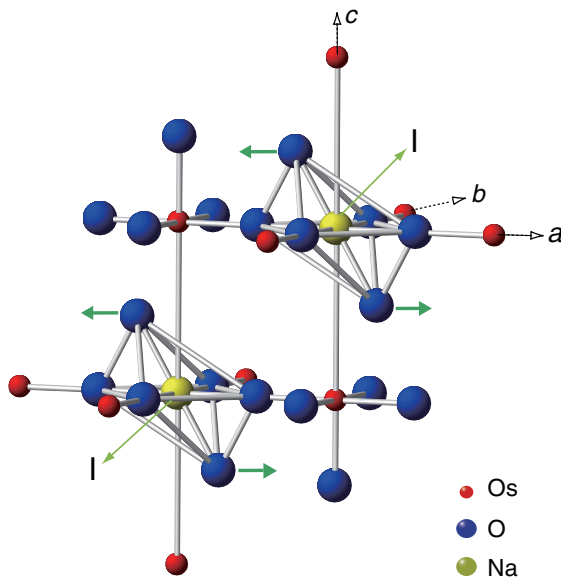

FIG. 10. Schematic of the tilt-lattice distortion. One structurally distinct Na site in noncubic environment is produced by tilt of the (a,c) plane. (Model D)
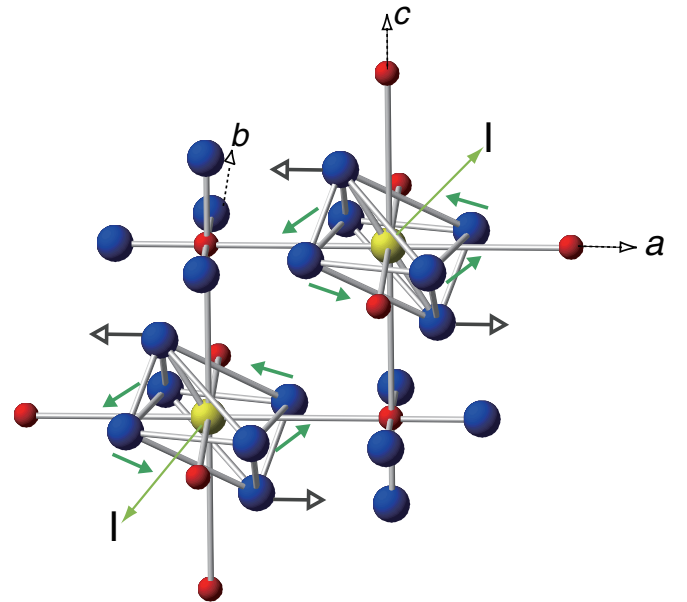

FIG. 11. Schematic of the combined rotational and tilt lattice distortions. One structurally distinct Na site in noncubic environment is induced by concurrent (a,b) plane rotation and (a,c) plane tilt. (Model E)

TABLE VI. Sample results of point charge calculations of rotational distortions in the (a,b) plane and tilt in the (a,c) plane. (Model E)

θ	ϕ	η	v_{aa}	v_{bb}	v_{cc}	δ_q(kHz)	V_{zz}
6.8°	20°	0.8194	−36.26	−3.6	39.86	189.11	c
7.1°	19°	0.859	−36.63	−2.779	39.41	190.68	c
7.3°	18°	0.8962	−36.69	−2.008	38.69	190.69	c
7.5°	17°	0.9342	−36.78	−1.251	38.03	190.98	c
7.6°	16°	0.9701	−36.51	−0.5546	37.07	189.52	c
7.8°	15°	0.991	−36.67	0.165	36.51	189.47	a
8.2°	14°	0.9493	−37.7	0.9555	36.75	190.79	a
8.5°	13°	0.9126	−38.41	1.677	36.73	190.83	a
8.7°	**12°**	**0.88**	**−38.74**	**2.324**	**36.41**	**189.38**	**a**
9°	11°	0.8489	−39.58	2.99	36.59	190.52	a
9.2°	10°	0.8214	−40.02	3.573	36.45	190.09	a

distortions involve changes in symmetry and global detectable changes of lattice parameters. A typical distortion mechanism involves a tilting of essentially rigid oxygen polyhedra, as is the case in $GdFeO_3$. In Ba_2NaOsO_6 this type of modification would tilt the entire rigid oxygen octahedra surrounding the Na ion. In this case, rigid implies that the octahedra preserve their shape, i.e., no independent motion of individual oxygen atoms occurs. However, the orientation of the entire octahedra changes as it tilts away from the [001] direction. The tilt is characterized by two angles: θ, referred to as the polar angle away from the c axis, and ϕ, the azimuthal angle defined relative to the a axis, as illustrated in Fig. 12(a). The tilted crystal structure is depicted in Fig. 13 and corresponds to $a^+a^+c^+$ distortion in Glazer's notation, i.e., the $Pmmn$ space group, as explained in Appendix C. The important thing about the $GdFeO_3$-type
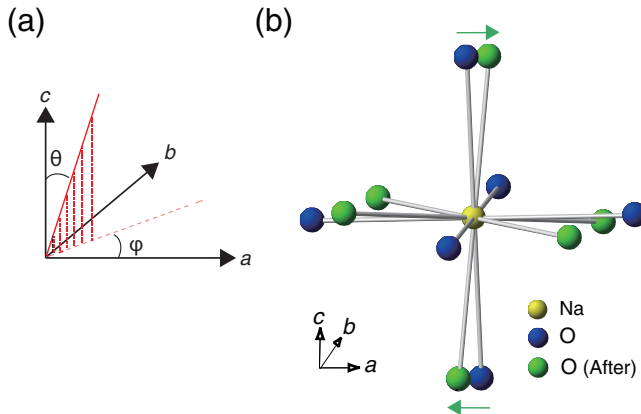

(a)　　(b)

FIG. 12. Schematic of the proposed $GdFeO_3$-type distortion. (a) The red solid line denotes distorted Na-O bond, which in its undistorted state points along the c axis. The NaO_6 octahedra is tilted by angle θ and ϕ in spherical coordinates. (b) Schematic of the specific tilt of NaO_6. The blue spheres/atoms represent O^{2-} ions in the undistorted state while the green ones represent distorted ones. We note that ϕ is the angle in the (a,b) plane but the four oxygen ions, originally in the (a,b) plane, are no longer in that plane after the distortion. This corresponds to $a^+a^+c^+$ distortion in Glazer's notation. (Model F)
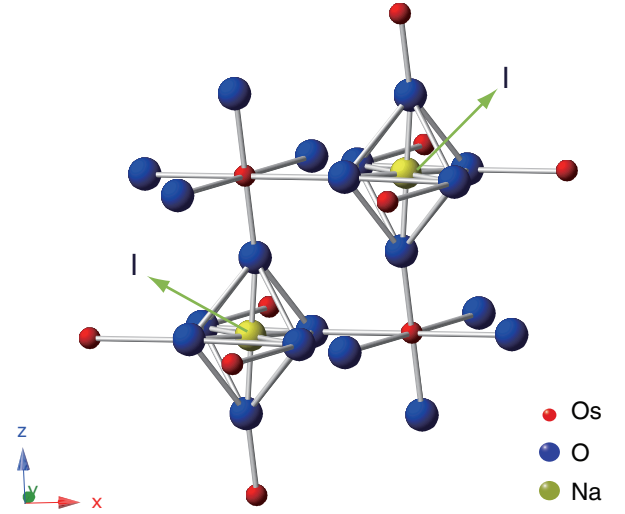

FIG. 13. Tilting of essentially rigid oxygen octahedra. The schematic of the tilting of NaO_6 octahedra with $\theta = 10°$ and $\phi = 45°$, where θ and ϕ are standard angles defining spherical coordinates. (Model F_2)

distortion is that only the orientation of the octahedra changes, whereas their intraionic structure remains intact. Moreover, typical values of the bend in the bond involving oxygen in $GdFeO_3$ are roughly between 145–170°. Point charge calculations are carried for both rigid and nonrigid octahedra cases. As it results from our calculations, the maximum quadrupole splitting induced by the distortions involving rigid octahedra does not exceed ≈150 kHz. A subset of the results is displayed in Table VII. Besides insufficient magnitude of the splitting, in all cases we obtain $V_{zz} \| c$, inconsistent with observations.

Next, we consider the flexible octahedra, where the intraoxygen bonds within an octahedra can either elongate or compress, like in models A and B. To illustrate this, we take the second entry of Table I. This entry corresponds to 0.55% elongation along the a axis, 0.1% elongation along the b axis, and 0.25% compression along the c axis, which generates calculated results in agreement with observations. We then combine such elongation/compression and the rigid tilt. In Model A, the displacement of Na-O bond occurs along the a, b, or c axis. As the octahedra tilt, the displacements are still along

TABLE VII. Sample results of point charge calculations of $GdFeO_6$-type distortion with rigid O_6 octahedra. (Model F)

θ	ϕ	η	v_{aa}	v_{bb}	v_{cc}	δ_q(kHz)	V_{zz}
0°	10°	0	−2.465	−2.465	4.93	18.091	c
0°	30°	0	−15.46	−15.46	30.92	113.46	c
0°	46°	0	−20.63	−20.63	41.25	151.39	c
0°	60°	0	−15.46	−15.46	30.92	113.46	c
2°	10°	0.0721	−2.577	−2.23	4.807	17.687	c
2°	30°	0.0067	−15.49	−15.29	30.78	112.96	c
2°	46°	0.0004	−20.54	−20.56	41.1	150.85	c
6°	46°	0.0031	−19.96	−20.08	40.03	146.92	c
10°	46°	0.0086	−18.85	−19.17	38.02	139.55	c

TABLE VIII. Sample results of point charge calculations of $GdFeO_6$-type distortion with flexible NaO_6 octahedra (Model F + Model A). The underlying distortions along the a, b, and c axis are 0.55%, 0.1% and 0.25%. The calculated η and δ_q are symmetric with respect to $\phi = 45°$ because the a axis and b axis are symmetric around $\phi = 45°$. (Model F_2)

θ	ϕ	η	v_{aa}	v_{bb}	v_{cc}	δ_q (kHz)	V_{zz}
0°	**0°**	**0.8768**	**38.89**	**−2.395**	**−36.49**	**189.81**	**a**
0°	**2°**	**0.8719**	**38.71**	**−2.479**	**−36.24**	**188.51**	**a**
0°	10°	0.7814	35.17	−3.844	−31.32	163.8	a
0°	44°	0.2214	−2.675	−4.196	6.87	25.825	c
0°	46°	0.2214	−4.196	−2.675	6.87	25.825	c
2°	**0°**	**0.8694**	**39.13**	**−2.555**	**−36.58**	**190.31**	**a**
2°	**2°**	**0.8646**	**38.96**	**−2.638**	**−36.32**	**189**	**a**
2°	44°	0.2274	−2.612	−4.149	6.761	25.445	c
2°	46°	0.2274	−4.149	−2.612	6.761	25.445	c
4°	**2°**	**0.8452**	**39.58**	**−3.063**	**−36.52**	**190.2**	**a**
4°	44°	0.2447	−2.442	−4.025	6.468	24.436	c
4°	46°	0.2447	−4.025	−2.442	6.468	24.436	c

the Na-O bonds but no longer along the principal axes of the crystal. As in the case of rigid octahedra, θ and ϕ are the polar and azimuthal angles in spherical coordinates as depicted in Fig. 12(a). A subset of point charge calculation results is shown in Table VIII. Minimum splitting occurs when $\phi = 45$ for fixed θ. As illustrated in Table VIII, to generate results compatible with our observations, we find that the displacements of oxygen ions must be comparable to those that reproduce the data in Model A and the angles do not exceed 4°. Such a small tilt angle induces a displacement of oxygen ions that is much smaller than the dominant displacement along the cubic axes of the perovskite reference unit cell. For angles larger than 4°, both δ_q and η significantly decrease below the observed value. Larger angle displacements along the cubic axes are required to obtain desired δ_q and η values in agreement with the data. This indicates that the dominant displacement of oxygen ions along the cubic axes of the perovskite reference unit cell reproduce our observations, as was the case described in Model A. Essentially, this model maps to Model A. In addition, the tilt angle has to remain relatively small to assure that these distortions induce and EFG with the principal axes aligned with those of the crystal, as imposed by the experiment. Therefore, $GdFeO_3$-type tilt distortions are inconsistent with our data.

VI. CONCLUSION

We reviewed details of the quadrupole interactions in Ba_2NaOsO_6 in the low temperature phase characterized by local cubic symmetry breaking. We presented measurements of the splitting δ_q, frequency difference between the adjacent quadrupole perturbed Zeeman energy levels, at 15 T and 8 K as a function of the direction of the applied magnetic field. The field was rotated away from the [001] crystalline axis in two different planes of the crystal. From the analysis of the rotation data in two different planes, we established that only the orthorhombic distortions are responsible for the local cubic symmetry breaking in the low temperature magnetically ordered phase. These distortions induce an EFG with principal

axes aligned with those of the crystal, a principal component $V_{zz} \| a$, and an anisotropy parameter of $\eta \approx 0.87$.

To find the full set of possible distortions that can induce such EFG, we employed the point charge model to calculate V_{zz} and η resulting from different scenarios. This is the simplest model valid for strongly ionic compounds, such as Ba_2NaOsO_6. However, it allowed us to quickly scan through a huge parameter space of possible lattice modifications. We found that our experimental observations can be accounted for by distortions of oxygen octahedra surrounding Na ions dominated by the displacement of oxygen ions along the cubic axes of the perovskite reference unit cell, as described in Model A. In addition to distortions in Model A, we find that Model E consisting of combined affects of tilt distortions in the (a,c) plane with rotational distortions in the (a,b) plane, for angles not exceeding 12°, is consistent with our data. Both models are characterized by the dominant displacement of oxygen ions along the cubic axes of the perovskite reference unit cell.

Since we cannot distinguish between displacements of the actual ions and distortions of the ion charge density, the point charge approach does not allow us to determine the nature of the orbital order possibly responsible for the local cubic symmetry breaking in Ba_2NaOsO_6 described in Ref. [2]. First principle calculations [28,29] of the EFG, with the input from our current work, are required to learn more about the nature of the putative orbital order in this compound.

As indicated in Ref. [10], the presence of a two-sublattice canted ferromagnetic state can imply that the broken cubic symmetry phase is a staggered quadrupolarly ordered phase with distinct orbital polarization on two sublattices. Experimentally, the distinct orbital polarization on two sublattices, and thus the exact nature of the orbital order, can directly be identified by performing ^{17}O NMR. The challenge in such an experiment is the weakness of naturally abundant ^{17}O NMR signal, but this can be overcome by performing ^{17}O isotope exchange.

APPENDIX A: QUADRUPOLE INTERACTION

1. Axially Symmetric Case

In the simplest case of a field with axial symmetry, the interaction between the EFG (eq) and the nucleus with spin I and quadrupole moment eQ, is described by the quadrupole Hamiltonian,

$$\mathcal{H}_Q = \frac{(eQ)(eq)}{4I(2I-1)}\left[3I_z^2 - I(I+1)\right]. \quad (A1)$$

By definition the EFG is a 3×3 tensor that corresponds to the rate of change of the electric field at an atomic nucleus [19]. The matrix is symmetric and traceless. The principal components are denoted by V_{xx}, V_{yy}, V_{zz}, and $|V_{zz}| \geqslant |V_{yy}| \geqslant |V_{xx}|$. By convention, the principal component of the EFG is defined as $V_{zz} \equiv eq$. The principal axes of the EFG define the coordinate system O_{XYZ}, which is not necessarily aligned with that defined by the crystallographic axes O_{xyz}. Evidently, V_{zz} is parallel to one of the crystal axes if the principal axes of the EFG and those of the crystal are aligned.

For a nuclear spin $I = 3/2$, as is the case of ^{23}Na, the energy eigenstates of $\mathcal{H}_Q$ are given by

$$E_m = \frac{(eQ)(eq)}{4I(2I-1)}[3m^2 - I(I+1)]. \quad \text{(A2)}$$

Then, the frequencies between different quadrupole satellite transitions equal

$$\omega_{m \to m-1} = \frac{(eQ)(eq)}{h\,4I(2I-1)}[3(2m-1)] = \frac{(eQ)(eq)}{h} \times \Omega$$

$$\Omega \equiv \frac{1}{2}, \quad \text{for} \quad |+3/2\rangle \to |+1/2\rangle$$

$$0, \quad \text{for} \quad |+1/2\rangle \to |-1/2\rangle$$

$$-\frac{1}{2}, \quad \text{for} \quad |-1/2\rangle \to |-3/2\rangle. \quad \text{(A3)}$$

Therefore, in a magnetic field applied along the principal axis of the EFG only three NMR lines (transitions) will be observed with equal splitting δ_q between adjacent transitions. In this case, the quadrupole splitting δ_q between different quadrupole satellites is simply given by

$$\delta_q = \frac{1}{2h}(eQ)(V_{zz})$$

$$= \frac{1}{2h}(\text{Quadrupole moment}) \times (\text{EFG}). \quad \text{(A4)}$$

Consequently, we can estimate the value of the EFG by using the experimentally determined value of the splitting $\delta_q \approx 190$ kHz for $H \| [001]$.

$$\text{EFG} = \frac{2h\delta_q}{eQ}$$

$$= \frac{2 \times 4.136 \times 10^{-15}\,\text{eV} \cdot s \times 190 \times 10^3\,\text{s}^{-1}}{0.12 \times e \times 10^{-28}\,\text{m}^2}$$

$$= 1.31 \times 10^{20}\,\text{V/m}^2. \quad \text{(A5)}$$

Next, this value can be used to roughly estimate the magnitude of particular lattice distortions in our material. In the oxygen octahedra surrounding the Na nuclei the EFG takes on the following form [30],

EFG

$$= \frac{2q}{4\pi\epsilon_0}\begin{bmatrix} \frac{2}{a^3} - \frac{1}{b^3} - \frac{1}{c^3} & 0 & 0 \\ 0 & -\frac{1}{a^3} + \frac{2}{b^3} - \frac{1}{c^3} & 0 \\ 0 & 0 & -\frac{1}{a^3} - \frac{1}{b^3} + \frac{2}{c^3} \end{bmatrix}. \quad \text{(A6)}$$

Clearly, with cubic symmetry such as in $\text{Ba}_2\text{NaOsO}_6$, the paramagnetic state is characterized by $a = b = c$. The

EFG is then zero, which leads to a vanishing splitting δ_q.

The observed δ_q is largest for a field applied in the [001] direction, as shown in Fig. 2 of the main text. In this case the simplest model, accounting for the splitting of the Na line into three equally spaced quadrupole satellite lines, involves distortions of the O octahedra surrounding Na nuclei solely along the [001] direction. In this case, $q = 2e$, $a = b \neq c$, and we obtain

$$\text{EFG} = \frac{2q}{4\pi\epsilon_0}\begin{bmatrix} \frac{1}{a^3} - \frac{1}{c^3} & 0 & 0 \\ 0 & \frac{1}{a^3} - \frac{1}{c^3} & 0 \\ 0 & 0 & -2(\frac{1}{a^3} - \frac{1}{c^3}) \end{bmatrix}. \quad \text{(A7)}$$

Therefore, the principal axis of the EFG ($V_{zz} \equiv eq$) is given by

$$V_{zz} = \pm\frac{8e}{4\pi\epsilon_0}\left(\frac{1}{a^3} - \frac{1}{c^3}\right) \quad \text{(A8)}$$

$$\left(\frac{1}{a^3} - \frac{1}{c^3}\right) = \pm\frac{4\pi\epsilon_0}{8e} \times 1.31 \times 10^{20}\,\text{V/m}^2$$

$$= \pm 0.01137 \times 10^{30}\,\text{m}^{-3}. \quad \text{(A9)}$$

In $\text{Ba}_2\text{NaOsO}_6$ with $a = 2.274$ Å, distortions along the c crystalline axis of the order of 4% can account for the observed δ_q, that is

$$\frac{1}{c^3} = \frac{1}{a^3} \pm 0.01137$$

$$c = 2.181\text{Å} \quad (-4.1\%), \quad \text{for compression}$$

$$c = 2.385\text{Å} \quad (4.9\%), \quad \text{for elongation}. \quad \text{(A10)}$$

2. Anisotropic Charge Distribution Case

For anisotropic charge distributions, the quadrupole Hamiltonian expressed in the coordinate system defined by the principal axes of the EFG is given by

$$\mathcal{H}_Q(x,y) = \frac{eQV_{zz}}{4I(2I-1)}\left[(3\hat{I}_z^2 - \hat{I}^2) + \eta(\hat{I}_x^2 - \hat{I}_y^2)\right], \quad \text{(A11)}$$

where $\eta \equiv (V_{xx} - V_{yy})/V_{zz}$ is the asymmetry parameter and V_{xx}, V_{yy}, and V_{zz} are diagonal components of the EFG. In this case, the splitting between the adjacent transitions is given by

$$\delta_q = \frac{(eQ)(V_{zz})}{2h}\left(1 + \frac{\eta^2}{3}\right)^{1/2}. \quad \text{(A12)}$$

Thus, the value of δ_q is dictated by both V_{zz} and anisotropy parameter η. In the high field limit, when $\mathcal{H}_Q$ is a perturbation to the dominant Zeeman term, the angular dependence of the splitting is given by

$$\delta_q = \frac{\nu_q}{2}(3\cos^2\theta - 1 + \eta\sin^2\theta\cos 2\phi), \quad \text{(A13)}$$

where θ is the angle between the applied field H and V_{zz}, ϕ is the standard azimuthal angle of spherical coordinate system defined by O_{XYZ}, and $\nu_Q \equiv \frac{3e^2qQ}{2hI(2I-1)} = \frac{(eQ)V_{zz}}{2h}$. As in the case of axially symmetric EFG, in the coordinate system defined by the principal axes of the EFG, denoted by (O_{XYZ}), only three NMR lines (transitions) will be observed with equal splitting δ_q between any adjacent lines.

APPENDIX B: LATTICE SUM

Considering the periodic nature of crystal structure, one determines the lattice in a standard way by the translation of the three primary vectors. We define the target Na site to be the origin of a three-dimensional coordinate system. Any other point in the lattice is denoted by

$$\boldsymbol{r}' = \boldsymbol{r} + \mu_1 \boldsymbol{a}_1 + \mu_2 \boldsymbol{a}_2 + \mu_3 \boldsymbol{a}_3, \tag{B1}$$

where $\boldsymbol{a}_i$ are the primary vectors of the lattice and μ_i the primary indices of these vectors. Then each atom within a unit cell can numerically be located from

$$\boldsymbol{r}_i = x_i \boldsymbol{a}_1 + y_i \boldsymbol{a}_2 + z_i \boldsymbol{a}_3, \tag{B2}$$

where x_i, y_i, and z_i are fractions between 0 and 1 that represent the position of the ith atom corresponding to the basis origin. Combining Eq. (B1) and Eq. (B2), the position of any particular ion is then given by

$$\boldsymbol{r}_i = (\mu_1 + x_i)\boldsymbol{a}_1 + (\mu_2 + y_i)\boldsymbol{a}_2 + (\mu_3 + z_i)\boldsymbol{a}_3. \tag{B3}$$

APPENDIX C: GLAZER'S NOTATION

Perovskite oxides are well known to be prone to lattice distortions [26,27]. In fact, most materials with perovskite structures are not in their ideal cubic form ABO_3, described by the $Pm\bar{3}m$ space group and represented as a network of corner-sharing BO_6 octahedra with 'A' atoms located in the geometric center of the gap between oxygen octahedra. However, their distorted structure can be defined as distortions from the ideal cubic configuration. The types of distortions established in perovskites can be reduced to three types: B-cation displacements within an octahedra, distortions of the BO_6 octahedral unit (Models: A, B, C, D, and E), and the rigid tilting of the corner-sharing BO_6 linked-octahedra units (Model F). This last type of distortion was classified and derived from crystallographic assumptions by Glazer in Ref. [31]. That is, Glazer type distortions are described in terms of tilt components along the three different pseudocubic (PC) axes, referred to the original undistorted cubic perovskite. Such pseudocubic axes coincide with the tetrad axes of the octahedra. Given the octahedra corner connections, a tilt about a pseudocubic axis determines the tilts in the directions perpendicular to this axis. However, the tilt of the successive octahedra along the same axis can be either in the same direction or in the opposite direction. To sum up, there are several possibilities for tilts in a perovskite network of corner-sharing octahedra: The main axis of the tilt can be parallel to each crystallographic axis; the amplitude of each tilt may be different from the others, and two subsequent layers being stacked along the tilt axis may be tilted either in phase or antiphase. The different possibilities of tilt distortions can be labeled by the notation $a^* b^* c^*$, where a, b, c refer to tilts around the $[100]_{PC}$, $[010]_{PC}$, and $[001]_{PC}$ axes, respectively. If letters are repeated, the tilts are equal for their respective axis. The superscript * can be either 0 for no tilt along an axis, $+$ for tilt of successive octahedra in the same sense, or $-$ for tilt of successive octahedra in the opposite sense [31,32].

[1] W. Witczak-Krempa, G. Chen, Y. B. Kim, and L. Balents, Correlated quantum phenomena in the strong spin-orbit regime, Annu. Rev. Condens. Matter Phys. **5**, 57 (2014).

[2] G. Chen, R. Pereira, and L. Balents, Exotic phases induced by strong spin-orbit coupling in ordered double perovskites, Phys. Rev. B **82**, 174440 (2010).

[3] G. Jackeli and G. Khaliullin, Mott Insulators in the Strong Spin-Orbit Coupling Limit: From Heisenberg to a Quantum Compass and Kitaev Models, Phys. Rev. Lett. **102**, 017205 (2009).

[4] G. Chen and L. Balents, Spin-orbit coupling in d^2 ordered double perovskites, Phys. Rev. B **84**, 094420 (2011).

[5] T. Dodds, T.-P. Choy, and Y. B. Kim, Interplay between lattice distortion and spin-orbit coupling in double perovskites, Phys. Rev. B **84**, 104439 (2011).

[6] W. S. Cole, S. Zhang, A. Paramekanti, and N. Trivedi, Bose-Hubbard Models with Synthetic Spin-Orbit Coupling: Mott Insulators, Spin Textures, and Superfluidity, Phys. Rev. Lett. **109**, 085302 (2012).

[7] C. Svoboda, M. Randeria, and N. Trivedi, Orbital and spin order in spin-orbit coupled d^1 and d^2 double perovskites, arXiv:1702.03199.

[8] J. Romhányi, L. Balents, and G. Jackeli, Spin-Orbit Dimers and Noncollinear Phases in d^1 Cubic Double Perovskites, Phys. Rev. Lett. **118**, 217202 (2017).

[9] H. Ishizuka and L. Balents, Magnetism in $S = \frac{1}{2}$ double perovskites with strong spin-orbit interactions, Phys. Rev. B **90**, 184422 (2014).

[10] L. Lu, M. Song, W. Liu, A. P. Reyes, P. Kuhns, H. O. Lee, I. R. Fisher, and V. F. Mitrović, Magnetism and local symmetry breaking in a Mott insulator with strong spin orbit interactions, Nat. Commun. **8**, 14407 (2017).

[11] W. Liu, R. Cong, E. Garcia, A. P. Reyes, H. O. Lee, I. R. Fisher, and V. F. Mitrović, Phase diagram of Ba$_2$NaOsO$_6$, a Mott insulator with strong spin orbit interactions, Physica B **536**, 863 (2018).

[12] M. H. Cohen and F. Reif, Quadrupole effects in nuclear magnetic resonance studies of solids, Solid State Phys. **5**, 321 (1957).

[13] E. N. Kaufmann and R. J. Vianden, The electric field gradient in noncubic metals, Rev. Mod. Phys. **51**, 161 (1979).

[14] A. D. Bain and M. Khasawneh, From NQR to NMR: The complete range of quadrupole interactions, Concepts Magn. Reson. Part A **22A**, 69 (2004).

[15] T. Kiyama and M. Itoh, Presence of 3d Quadrupole Moment in LaTiO$_3$ Studied by 47,49Ti NMR, Phys. Rev. Lett. **91**, 167202 (2003).

[16] C. Berthier, NMR study on a 2H-NbSe$_2$ single crystal: A microscopic investigation of the charge density waves state, J. Phys. C **11**, 797 (1978).

[17] Y. Tokunaga, D. Aoki, Y. Homma, S. Kambe, H. Sakai, S. Ikeda, T. Fujimoto, R. E. Walstedt, H. Yasuoka, E. Yamamoto, A. Nakamura, and Y. Shiokawa, NMR Evidence for Higher-Order Multipole Order Parameters in NpO$_2$, Phys. Rev. Lett. **97**, 257601 (2006).

[18] A. Abragam, *Principles of Nuclear Magnetism* (Oxford University Press, Oxford, 1996), pp. 216–263.

[19] C. P. Slichter, *Principles of Magnetic Resonance* (Springer, Berlin, 1996), pp. 485–502.

[20] For rotations in the $(1\bar{1}0)$ plane, we did not confirm the local maximum of the splitting for a field applied parallel to the [110] direction because of the NMR coil and goniometer geometry.

[21] Z. Islam (private communication).

[22] A. S. Erickson, S. Misra, G. J. Miller, R. R. Gupta, Z. Schlesinger, W. A. Harrison, J. M. Kim, and I. R. Fisher, Ferromagnetism in the Mott Insulator Ba_2NaOsO_6, Phys. Rev. Lett. **99**, 016404 (2007).

[23] K. E. Stitzer, M. D. Smith, and H.-C. zur Loye, Crystal growth of Ba_2MOsO_6 (M=Li, Na) from reactive hydroxide fluxes, Solid State Sci. **4**, 311 (2002).

[24] K.-W. Lee and W. E. Pickett, Orbital-quenching–induced magnetism in Ba_2NaOsO_6, Europhys. Lett. **80**, 37008 (2007).

[25] P. Herzig, Electrostatic potentials, fields and field gradients from a general crystalline charge density, Theor. Chim. Acta **67**, 323 (1985).

[26] K. S. Aleksandrov and J. Bartolome, Structural distortions in families of perovskite-like crystals, Phase Transitions **74**, 255 (2001).

[27] J.-S. Zhou and J. B. Goodenough, Intrinsic structural distortion in orthorhombic perovskite oxides, Phys. Rev. B **77**, 132104 (2008).

[28] A. B. Harris, Landau theory of tilting of oxygen octahedra in perovskites, Phys. Rev. B **85**, 174107 (2012).

[29] K. Z. Rushchanskii, N. A. Spaldin, and M. Ležaić, First-principles prediction of oxygen octahedral rotations in perovskite-structure $EuTiO_3$, Phys. Rev. B **85**, 104109 (2012).

[30] Sung Ho Choh, Hee Won Shin, II-Woo Park, Heongkyu Ju, Jong Hyun Kim, and Hae Jin Kim, Calculation of electric field gradient tensor for simple point charge distributions and its application to real systems, Journal of the Korean Magnetic Resonance Society **7**, 16 (2003).

[31] A. M. Glazer, The Classification of Tilted Octahedra in Perovskites, Acta Crystallogr. B **28**, 3384 (1972).

[32] A. M. Glazer, Simple Ways of Determining Perovskite Structures, Acta Crystallogr. A **31**, 756 (1974).